A&A, 683, A132 (2024)
https://doi.org/10.1051/0004-6361/202347635

Astronomy & Astrophysics

LOFAR detection of extended emission around a mini halo in the galaxy cluster Abell 1413

G. Lusetti[1,2], A. Bonafede[2], L. Lovisari[7,8], M. Gitti[2], S. Ettori[3], R. Cassano[4], C. J. Riseley[2,4,5], F. Govoni[12], M. Brüggen[1], L. Bruno[2,4], R. J. van Weeren[6], A. Botteon[4], D. N. Hoang[1], F. Gastaldello[9], A. Ignesti[10], M. Rossetti[9], and T. W. Shimwell[11]

[1] Hamburger Sternwarte, University of Hamburg, Gojenbergsweg 112, 21029 Hamburg, Germany
e-mail: giulia.lusetti@hs.uni-hamburg.de
[2] DIFA – Università di Bologna, Via Gobetti 93/2, 40129 Bologna, Italy
[3] INAF – Osservatorio di Astrofisica e Scienza dello Spazio di Bologna, Via Piero Gobetti 93/3, 40129 Bologna, Italy
[4] INAF – Istituto di Radioastronomia di Bologna, Via Gobetti 101, 40129 Bologna, Italy
[5] CSIRO Space & Astronomy, PO Box 1130, Bentley, WA 6102, Australia
[6] Leiden Observatory, Leiden University, PO Box 9513, 2300 RA Leiden, The Netherlands
[7] INAF, Istituto di Astrofisica Spaziale e Fisica Cosmica di Milano, Via A. Corti 12, 20133 Milano, Italy
[8] Center for Astrophysics | Harvard & Smithsonian, 60 Garden Street, Cambridge, MA 02138, USA
[9] INAF – IASF Milano, Via A. Corti 12, 20133 Milano, Italy
[10] INAF – Padova Astronomical Observatory, Vicolo dell'Osservatorio 5, 35122 Padova, Italy
[11] ASTRON, Netherlands Institute for Radio Astronomy, Oude Hoogeveensedijk 4 7991 PD, Dwingeloo, The Netherlands and Leiden Observatory, Leiden University, PO Box 9513, 2300 RA Leiden, The Netherlands
[12] INAF – Osservatorio Astronomico di Cagliari, Via della Scienza 5, 09047 Selargius (CA), Italy

Received 2 August 2023 / Accepted 1 December 2023

ABSTRACT

Context. The relation between giant radio halos and mini halos in galaxy clusters is not understood. The former are usually associated with merging clusters, while the latter are found in relaxed systems. In recent years, the advent of low-frequency radio observations has challenged this dichotomy by finding intermediate objects with a hybrid radio morphology.
Aims. We aim to investigate the presence of diffuse radio emission in the cluster Abell 1413 and determine its dynamical status to explore the relation between mini halos and giant radio halos.
Methods. We used LOFAR observations centred at 144 MHz to study the diffuse radio emission. To investigate the dynamical state of the system, we used newly analysed *XMM-Newton* archival data. Abell 1413 shows features that are typically present in both relaxed (e.g., peaked X-ray surface brightness distribution and some large-scale inhomogeneities) and disturbed (e.g., flatter temperature and metallicity profiles) clusters.
Results. This suggests that Abell 1413 is neither disturbed nor fully relaxed, and we argue that it is an intermediate-phase cluster. At 144 MHz, we discover a wider diffuse component surrounding the previously known mini halo at the cluster center. By fitting the radio surface-brightness profile with a double-exponential model, we can disentangle the two components. We find an inner mini halo with an *e*-folding radius, $r_{e,1} = 28 \pm 5$ kpc, and an extended component with $r_{e,2} = 290 \pm 60$ kpc. We also evaluated the point-to-point correlation between the radio and X-ray surface brightness, finding a sublinear relation for the outer emission and a superlinear relation for the mini halo. The mini halo and the diffuse emission extend over different scales and show different features, confirming the double nature of the radio emission and suggesting that the mechanisms responsible for the re-acceleration of the radio-emitting particle might be different.

Key words. radiation mechanisms: non-thermal – radiation mechanisms: thermal – galaxies: clusters: individual: Abell 1413 – galaxies: clusters: intracluster medium – radio continuum: general

1. Introduction

Galaxy clusters have a size that ranges from a few hundreds of kpc to, approximately, Mpc, and have typical masses of 10^{14}–$10^{15}\,M_{\odot}$. They can contain up to 1000 galaxies, embedded in the intracluster medium (ICM). The ICM consists of fully ionized hydrogen and helium and traces of highly ionized heavier elements with a temperature $T \sim 10^{7}$–10^{8} K (1–10 keV) and particle number densities steeply declining from $n_{\rm e} \sim 10^{-2}$–10^{-3} cm^{-3} near the center to 10^{-4} cm^{-3} in the outskirts. It emits mainly via thermal bremsstrahlung in the X-ray band (e.g., Forman & Jones 1982; Sarazin 2009).

Co-spatially with the ICM, an increasing number of galaxy clusters is also observed to host diffuse nonthermal synchrotron emission, with no obvious connection to the individual cluster members. The synchrotron emission reveals the presence of magnetic field and relativistic cosmic-ray electrons (CRes) in the ICM. Extended, central, diffuse sources are usually classified as giant radio halos and mini halos (see van Weeren et al. 2019 for a review). Both giant and mini halos exhibit steep spectrum[1] with a spectral index $\alpha > 1$. While giant radio halos are Mpc-sized radio sources which cover large parts of the cluster volume, mini halos are typically confined within the cool cores (~300–500 kpc) of relaxed galaxy clusters and are characterized by higher emissivity (e.g., Cassano et al. 2008; Murgia et al. 2009).

[1] The synchrotron radio spectrum is defined as $S(\nu) \propto \nu^{-\alpha}$.

Two emission mechanisms have been proposed to explain these nonthermal radio sources (see Brunetti & Jones 2014 for a review): (i) the (re-)acceleration scenario, where CRes are (re-) accelerated by turbulence that develops during cluster mergers; (ii) the hadronic scenario, where secondary CRes are produced by proton-proton collisions between relativistic cosmic-ray protons (CRps) and thermal protons in the ICM. While it has been shown that purely hadronic models cannot reproduce the emission of giant radio halos (Brunetti et al. 2008, 2017), they remain a viable mechanism for mini halos (Pfrommer & Enßlin 2004; Jacob & Pfrommer 2017). Statistical studies have shown the connection between the dynamical status of the cluster and the type of diffuse radio emission (e.g., Cassano et al. 2010, 2023; Cuciti et al. 2021). Galaxy clusters hosting giant halos are mainly characterized by a disturbed dynamical status, suggesting recent or ongoing mergers (e.g., Cassano et al. 2013; Cuciti et al. 2015). On the other hand, mini halos are usually found in relaxed cool-core clusters (Gitti et al. 2004, 2018; Cassano et al. 2010), but their origin is unclear since they could be of leptonic or hadronic origin (e.g., van Weeren et al. 2019). Moreover, in a statistical study about the occurrence of mini halos in a sample of massive ($M > 6 \times 10^{14}\,M_{\odot}$) galaxy clusters, Giacintucci et al. (2017) found that ∼80% of cool-core clusters (classified according to the value of central entropy $K_0 < 30\,\mathrm{keV\,cm^2}$) host a mini halo, suggesting a clear relation between the origin of mini halos and the properties of the cool-core gas.

In recent years, the advent of deep, low-frequency observations has complicated the picture described above. In fact, a few cool-core clusters show the presence of a diffuse synchrotron halo or halo-like emission that extends quite far from the central mini halo (Bonafede et al. 2014; Venturi et al. 2017; Sommer et al. 2017; Savini et al. 2018, 2019; Biava et al. 2021; Riseley et al. 2022b; Bruno et al. 2023a), challenging the idea that mini halos occur in cool-core clusters and giant halos in non-cool-core clusters. These peculiar galaxy clusters either present giant halos (Bonafede et al. 2014; Savini et al. 2018) or show a hybrid morphology in the radio emission (Biava et al. 2021), even though they are classified as relaxed systems based on their thermal properties. Until now, a somewhat unique case has been represented by the galaxy cluster RX J1720.1+2638 (Savini et al. 2019; Biava et al. 2021), where the radio emission is composed of a central bright mini halo plus fainter and wider emission, extending far from the cluster core. In this study, the authors showed that the radio diffuse emission presents different features, suggesting an intrinsically different nature of the two sources. An even more complex morphology has been found in Abell 2142, a galaxy cluster with an intermediate dynamical state, already known to host a hybrid radio halo with two distinct components (Venturi et al. 2017). This object has recently been studied with low-frequency radio observation by Bruno et al. (2023a), who detected a third ultra-steep spectrum and wider component. Only a handful of multi-component diffuse sources only are currently known, but their number may increase thanks to sensitive low-frequency observations.

In this work, we present the galaxy cluster Abell 1413 (hereafter A1413; *Planck* name: PSZ2 G226.18+76.79), which is a nearby ($z = 0.143$) massive ($M_{500} = 5.95^{+0.24}_{-0.25} \times 10^{14}\,M_{\odot}$, Planck Collaboration XXVII 2016) system. It is well studied in the optical (Castagné et al. 2012), X-ray (Pratt & Arnaud 2002), and radio (Govoni et al. 2001; Giacintucci et al. 2017; Savini et al. 2019) bands. These previous studies at different wavelengths showed that the properties of A1413 are intermediate between classical relaxed and merging clusters. From the morphological point of view, it shows a high ellipticity confirmed by both optical (Castagné et al. 2012) and X-ray (Pratt & Arnaud 2002) studies. The cluster is elongated approximately in the North-South direction (Fig. 7 of Castagné et al. 2012). Studying the galaxy number density distribution, Castagné et al. (2012) estimated the value of the cluster ellipticity $\epsilon \sim 0.35$ at large radii, increasing up to ∼0.8 at the cluster center $r < 1'$. While fitting the *XMM-Newton* image, they found values quickly converging toward $\epsilon \sim 0.27$, which is fully compatible with the global value of $\epsilon \sim 0.29$ derived by Pratt & Arnaud (2002) over the radial range $[3'-13']$. They argue that this discrepancy at large radii of the optical and X-ray ellipticity values is not surprising as the collisional gas relaxes more quickly within the cluster potential than the non-collisional galaxies and reaches a spherically symmetric distribution more rapidly. However, Castagné et al. (2012) also stressed that A1413 seems a rather extreme example of this effect. Moreover, by analyzing the velocity distribution of the cluster, they found a velocity offset of $450 \pm 210\,\mathrm{km\,s^{-1}}$ (i.e., 2σ significance) between the velocity of the central cD galaxy (Paturel et al. 1989), which is also among the brightest cluster galaxies (BCGs), and the mean cluster velocity. These authors argue that BCGs' velocity offsets are frequently found in clusters that are distant from equilibrium, for example during significant merging events. If this BCG velocity offset is confirmed, it would indicate that A1413 may potentially be in a non-fully relaxed dynamical state.

On the other hand, early X-ray studies (Pratt & Arnaud 2002; Vikhlinin et al. 2005; Baldi et al. 2007) classified this cluster as a relaxed system, with no obvious signatures of a recent merger. The lack of shocks or cold fronts has also been confirmed by Botteon et al. (2018), who explored a combination of different analysis approaches of X-ray observations to firmly detect and characterize edges in a sample of non-cool-core massive galaxy clusters. The *XMM-Newton* observation (Pratt & Arnaud 2002) does not provide strong evidence of a cool-core region, in contrast with the temperature profiles obtained with *Chandra* (Vikhlinin et al. 2005), with a cooling time in the innermost bin (∼50 kpc) of $t_{\mathrm{cool}} = 4.2 \pm 0.3$ Gyr (Baldi et al. 2007). These authors suggested that this could be related to the better resolution of *Chandra* compared to *XMM-Newton*. Finally, using common X-ray morphological parameters such as the concentration parameter (c, Santos et al. 2008) and the centroid shift (w, Poole et al. 2006; Mohr et al. 1995), A1413 has been classified as a relaxed system (Lovisari et al. 2017; Campitiello et al. 2022; Yuan et al. 2022). However, it also has a mixed morphology, such as elongated X-ray isophotes and a relatively flat X-ray profile near the center.

The first investigation of the radio emission in A1413 was performed by Govoni et al. (2009), who found a candidate mini halo at a frequency of 1.4 GHz. Later, A1413 was included in a mini halo statistical study of Giacintucci et al. (2017), who classified clusters according to the value of the specific central entropy K_0. Interestingly, A1413 was the only non-cool-core cluster ($K_0 = 64 \pm 8\,\mathrm{keV\,cm^2}$) of the whole sample hosting a (candidate) mini halo. The diffuse radio emission was then studied at a frequency of 144 MHz, in a study of non-merging galaxy clusters (Savini et al. 2019), confirming the presence of a mini halo with a linear size of ∼210 kpc and a total flux density of 40 ± 7 mJy. In a recent study of Riseley et al. (2023), the mini halo was studied with a combination of LOFAR at 144 MHz and MeerKAT at 1283 MHz observations. They measured a linear size of at least 449 kpc (and up to 584 kpc) at 1283 MHz, twice as large as previously measured by Govoni et al. (2009). From these past studies, a controversial and intriguing picture of

Table 1. Properties of A1413 derived from literature.

z	0.1427
RA (h, m, s)	11 55 18.9
Dec (°,′,″)	+23 24 31
$M_{500} \times (10^{14}\, M_\odot)$	$5.95^{+0.24}_{-0.25}$
K_0 (keV cm^2)	64 ± 8
c	$0.44^{+0.04}_{-0.04}$
w	$0.04^{0.02}_{0.01} \times 10^{-1}$

Notes. Redshift (z: Böhringer et al. 2000); equatorial coordinates (NASA ExtragalCatalog, Bade et al. 1998); mass within the radius that defines the sphere within which the cluster's density is 500 times the critical density at the cluster's redshift (M_{500}; Planck Collaboration XXVII 2016); central entropy (K_0; Giacintucci et al. 2017); X-ray morphological parameter (c, w; Campitiello et al. 2022).

A1413 emerges, making it a very interesting object. In this paper, we present new radio observations performed with the LOFAR High Band Antennae (HBA) at 144 MHz. This is combined with archival and newly analyzed *XMM-Newton* data, which include a more accurate background treatment and improved calibration.

This paper is organised as follows. In Sect. 2 we give an overview of the observations and data reduction. The X-ray and radio results are presented in Sect. 3. We discuss the results from X-ray and radio analysis jointly in Sect. 4. In Sect. 5, we summarise our conclusions.

Throughout the paper we adopt a cosmology with $H_0 = 70\,\mathrm{km\,s^{-1}\,Mpc^{-1}}$, $\Omega_\Lambda = 0.7$ and $\Omega_\mathrm{m} = 0.3$. Thus, 1″ corresponds to a physical scale of 2.51 kpc at the redshift of A1413. A summary of the properties of A1413 collected from literature is reported in Table 1.

2. Observations and data reduction

In order to investigate the radio emission and dynamical state of A1413, we used LOFAR data at 144 MHz together with newly analysed archival data from the *XMM-Newton* telescope, the latter also being part of the CHEX-MATE program (CHEX-MATE Collaboration 2021). Moreover, we compare the LOFAR observation of the source with VLA image of this source presented in Govoni et al. (2009).

In the following sections, we describe these observations and the data reduction procedures. A summary of the observational details is reported in Table 2.

2.1. XMM-Newton

A1413 was observed with *XMM-Newton* four times between 2007 and 2008. All four observations were longer than 60 ks each. For this work, we retrieved the longest and least flared one, OBS ID 0502690201, from the *XMM-Newton* data archive (see Table 2). Data consist of 82.5 ks of archival observation time during *XMM-Newton* revolution 1466 (2007 December 11), obtained with the THIN1 filters and processed with XMM-SAS[2] v19.0.0 and the XMM-ESAS[3] software package (Snowden et al. 2008) and through a dedicated pipeline that follows the procedure described in Lovisari & Reiprich (2019) and is briefly described in this section. The pipeline processes the X-ray data from the raw data, the observation data file (ODF), passing through data calibration and filtering, imaging, and spectral fitting.

The raw data are initially processed using the `cifbuild` and `odfingest` tasks. The former provides an up-to-date list of the relevant calibration files, while the latter produces extended ODF summary file needed for subsequent data processing. Then, we run `emchain` and `epchain` tasks to convert the raw data into calibrated photon event files for the MOS and pn camera, respectively. We applied standard filtering procedures to discriminate events based on their pattern: only single, double, triple, and quadruple events for MOS (i.e., PATTERN ≤ 12) and single and double events for pn (i.e., PATTERN ≤ 4). We also performed bright pixels and hot column removal (i.e., FLAG==0) and removed the contamination by pn out-of-time events. Observation periods affected by high background due to soft protons (SP; see Sect. 2.1.1) were removed using a two-stage filtering process (see Lovisari et al. 2011 for details); these are summarised in the following. First, the light curve with 100 s bins is inspected in the [10–12] keV band for MOS and [12–14] keV for pn, since particle background dominates at high energy. The histogram of the light curve is then fit with a Poisson distribution, and time intervals with a higher count rate, i.e., a count rate that deviates by more than 2σ from the mean, are excluded (see Pratt & Arnaud 2002, Appendix A for a precise description). To obtain the final good time intervals (GTI), a second-stage filtering is performed, this time using the full [0.3–10] keV band in 10 s bins. This ensures a safety check for possible flares with soft spectra (e.g., Nevalainen et al. 2005).

Filtering the light curve does not ensure complete deletion of the SP contributions: continuous and constant flares (i.e., flares that last for long time intervals), without evident spikes, can still remain. We therefore estimate the amount of residual SP flare contamination by using the suitable code of De Luca & Molendi (2004). By comparing area-corrected count rates in the in- and out-of-field-of-view (FoV) regions of the detector, we find that the SP contamination is low[4], with a ratio of 1.12 ± 0.02 for all the cameras. Nevertheless, we included SP contamination as an extra model component when dealing with spectral fitting (Sect. 2.1.2). Anomalous behaviour of CCD 7 for MOS2 was detected via the `mos-filter` task (Kuntz & Snowden 2008) and excluded from this analysis, together with CCD 6 of MOS1, which was damaged by a meteorite in the early phase of the emission and thus is not available.

Point-like sources were detected with the `edetect-chain` task and visually inspected to distinguish between real point sources and extended cluster substructures before removing them from the event files. Even if it was identified as a point source, we did not remove the BCG region because the cluster emission is so bright that the contribution of the AGN is negligible and can be modeled as a power law during the spectral fitting.

2.1.1. Background treatment

The *XMM-Newton* EPIC background is made of several different components, each one with temporal, spectral, and spatial variations. It can be generally divided between particle and photon background.

[2] https://www.cosmos.esa.int/web/xmm-newton/sas
[3] https://heasarc.gsfc.nasa.gov/docs/xmm/xmmhp_xmmesas.html
[4] https://www.cosmos.esa.int/web/xmm-newton/epic-scripts

The main component of the photon background is the cosmic X-ray background (CXB), primarily consisting of unresolved cosmological sources, the Local Bubble, and the Galactic halo. To model the CXB, we used ROSAT All-Sky Survey[5] (RASS) diffuse background maps in a region beyond the cluster virial radius (between 1 and 2 deg) and fit it simultaneously with *XMM-Newton* data, as described in Lovisari & Reiprich (2019). We described the unresolved emission from AGNs via an absorbed power-law model with its slope set to 1.41 (De Luca & Molendi 2004); an absorbed ∼0.2 keV thermal component representing the Galactic halo (GH) emission, and an unabsorbed ∼0.1 keV component representing the Local Hot Bubble (LHB). During the fitting procedure, the temperature values of the LHB and GH thermal components are free to vary, while the slope of the AGN's power law is fixed.

The particle background includes signal generated by interactions of particles with the detectors and depends on the energy of the hitting particles. It can be divided between the quiescent particle background (QPB, with $E \gtrsim$ few MeV) and soft protons (SP, with $E < 100$ keV). QPB consists of a continuum component and fluorescent lines produced by the interaction of penetrating high energy particle with the detectors. We used filter wheel closed[6] (FWC) observations to estimate the intensity of QPB components. The model used for FWC observations consists of a broken power law with additional fluorescence lines (e.g., Fe, Al, Si, Au). Since FWC observations are taken from a different time period to our observation and have a different exposure, they need to be normalised, comparing them with the out-FoV data (unexposed corners of the CCD chips are a measure of the particle background level in each observation.). SP background is produced by relatively low energy protons accelerated in the Earth magnetosphere, passing through the telescope optics and depositing their energy directly on the CCDs. As described in Sect. 2.1, SP components are usually highly variable in time (ranging from ∼100 s to hours), and the enhancement in the count rate (referred to as flares) can be more than three orders of magnitude. This flare component is usually filtered via light-curve screening procedures, which are summarized in Sect. 2.1. Nonetheless, a more constant SP component can remain and contaminate the observations. To take into account this residual SP contamination, we added a power-law component, folded only with the redistribution matrix file, to the background modeling. We left both the slope and normalization free to vary for each detector and in the region of interest. This approximately accounts for the proton vignetting (which differs from the photon one, and for which there is no model available).

2.1.2. Spectral analysis

The spectral analysis is performed with the `XSPEC` (Arnaud et al. 1996) package v12.11.1, in the [0.5–12] keV and [0.5–14] keV energy range for MOS and pn, respectively. All the regions used for the spectral profiles were centered on the peak of the X-ray emission of coordinates RA(J2000) $11^{h}55^{m}17^{s}.85$ and Dec (J2000) $+23°24^{m}18^{s}.85$, and they extend until $R_{500} \sim 1224$ kpc (Planck Collaboration XXIX 2014). The sizes of the annuli were determined by requiring a minimum width of 30″ and a fixed $S/N = 50$. The first requirement ensures that most of the flux (i.e., >80%, Zhang et al. 2009) comes from the selected region (due to the *XMM-Newton* PSF, some photons scatter from one annulus to another); the second that the 1σ uncertainty in the spectrally resolved temperature (and consequently in the fit temperature profiles) is <10% (see Appendix B of Lovisari & Reiprich 2019 for more details on how uncertainties vary as a function of S/N and cluster temperature). The cluster emission is modeled with an `apec` single-temperature thermal plasma model with an absorption fixed at the total (neutral and molecular; see Willingale et al. 2013) $N_{\rm H} \sim 1.97 \times 10^{20}\,{\rm cm}^{-2}$ value estimated using the *Swift* online tool[7]. For the `apec` model (Smith et al. 2001), the parameters are plasma temperature [keV], metallicity, redshift (kept fixed at $z = 0.1427$), and the normalization $\frac{10^{-14}}{4\pi[D_{\rm A}(1+z)]^2}\int n_{\rm e} n_{\rm H} {\rm d}V$, with $D_{\rm A}$ being the angular distance of the source and $n_{\rm e}$,$n_{\rm H}$ the electron and proton densities in units of ${\rm cm}^{-3}$. In each annulus, the MOS and pn spectra were fit simultaneously and their normalizations left free to vary; this was done in order to account for the calibration offsets between the different detectors (e.g., Madsen et al. 2017). The background is modeled together with the cluster emission by performing a joint fit with the above explained RASS spectrum and FWC observations' components, and cluster emission extracted from each region.

2.2. LOFAR

The data used in this work are part of the LOFAR Two-metre Sky Survey (LoTSS; Shimwell et al. 2017, 2019, 2022), a sensitive (rms ∼ 100 μJy beam), high-resolution (full width at half maximum (FWHM) of the synthesised beam of ∼6″), low-frequency (120–168 MHz) radio survey of the northern sky. LoTSS observations are conducted with LOFAR (LOw Frequency Array: van Haarlem et al. 2013) high band antennas (HBA) in the `DUAL_INNER` mode configuration; each pointing consists of an 8 h observation book-ended by 10 min scans of the calibrator (3c395 for the observations used in this work), at the central frequency of 144 MHz and 48 MHz in total bandwidth. A1413 is covered by two pointings, P177+22, and P180+22.

Data have been calibrated following the LoTSS-DR2 pipeline (see Shimwell et al. 2022; Tasse et al. 2021 for details), which works on the direction-independent calibration products (i.e., 24 measurement sets for each pointing, which cover the 120–168 MHz band) and returns fully direction-dependent calibrated data. After calibration, the so-called extraction and self-calibration procedure (van Weeren et al. 2021) is performed: a region around the target of interest is selected and all the sources outside that region are subtracted using the direction-dependent gains obtained by the pipeline. The station beam is corrected for directly in the visibility space, and the phase center of the observation is shifted toward the direction of the target. This way, we are left with two data sets centered on the target that do not need any further beam correction. These two data sets are self-calibrated again to obtain more accurate calibration solutions in the region of interest. Self-calibration and imaging are done with DPPP and WSClean 2.10.0 (Offringa et al. 2014).

We re-imaged the self-calibrated data sets at different resolutions to classify the kind of radio emission and its properties. We always applied a Briggs (Briggs 1995) weighting scheme with a negative robust parameter, as it allows us to down-weight the secondary lobes, and inner *uv*-cut fixed at $b_{\rm min} > 80\lambda$

[5] Since in ROSAT observations, particle background is negligible, these can be considered as pure sky data. RASS diffuse background maps can be downloaded at the HEASARC web page `https://heasarc.gsfc.nasa.gov/cgi-bin/Tools/xraybg/xraybg.pl`.

[6] FWC exposures are taken with closed filters that avoid X-ray photons hitting the detector and thus are dominated by the instrumental background.

[7] `https://www.swift.ac.uk/analysis/nhtot/index.php`

Table 2. Observational overview: LOFAR HBA and VLA observations (top); X-ray observation (bottom).

Telescope	Central frequency	Configuration	On source time	Observation ID	Observation date	Reference
LOFAR	144 MHz	HBA_DUAL	8+8 h	591537, 602890	04.05.2017, 09.08.2017	(1)
VLA	1.4 GHz	C array	8 h		23.10.2006	(2)
Telescope	Energy range	Filter	On source time	Observation ID	Observation date	Reference
XMM-Newton	[0.5–14] keV	THIN1	82.5 ks	0502690201	11.12.2007, rev. # 1466	(1),(3)

References. (1) This work; (2) Govoni et al. (2009); (3) Pratt & Arnaud (2002).

Table 3. Radio images used in this work.

Telescope	Freq. [MHz]	Briggs weighting	Taper *FWHM* [″]	Resolution [″×″]	$\sigma_{\rm rms}$ [mJy beam^{-1}]	Reference
HBA	144	−1	–	4 × 6	0.15	Fig. 1 (left)
HBA	144	−0.25	20	35 × 35	0.27	Fig. 1 (right)
HBA	144	−0.25	10	15 × 15	0.18	Fig. 5 (left)

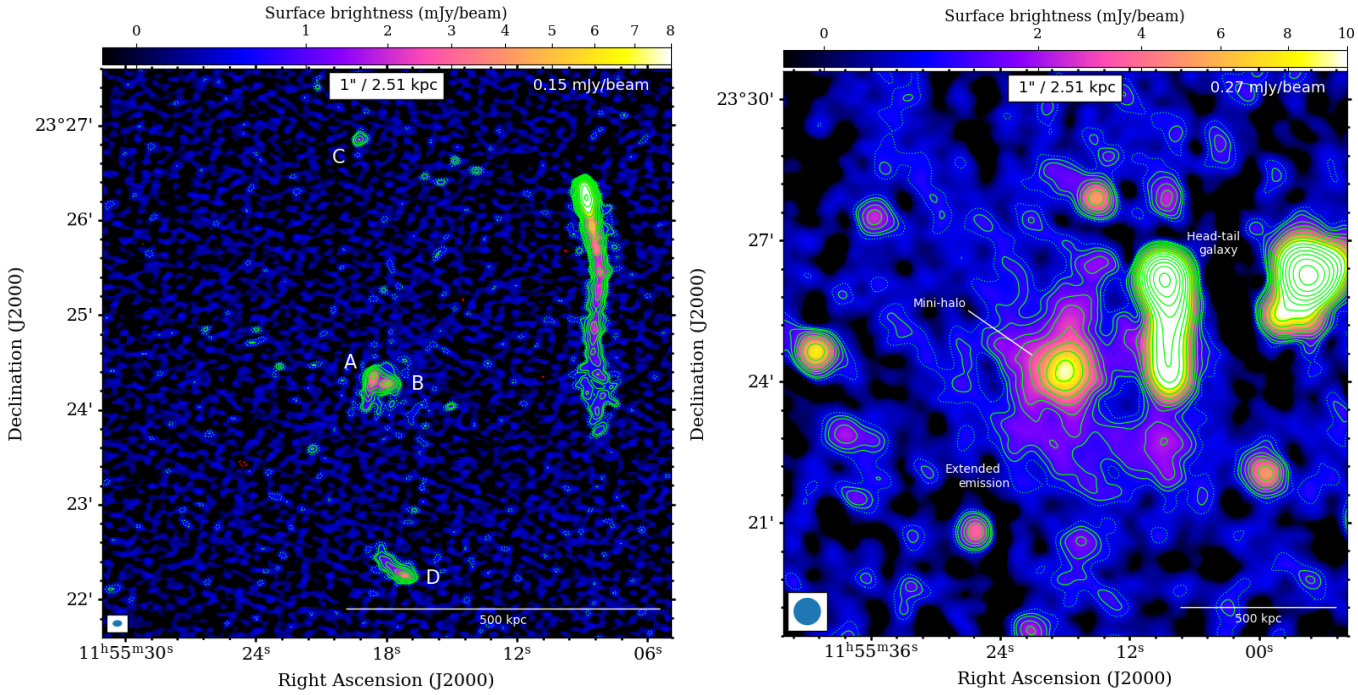

Fig. 1. High- and low-resolution radio images of A1413 at 144 MHz. Left panel: high resolution 144 MHz image with 4″ × 6″ beam (shown in the bottom left corner) and noise $\sigma_{\rm rms}$ = 0.15 mJy beam^{-1}. Sources that have been subtracted are labelled with letters: two central AGNs A, B; one point-like north source C and one extended south source D. Right panel: low-resolution source-subtracted 144 MHz image with 35″ × 35″ beam (shown in the bottom left corner) and noise $\sigma_{\rm rms}$ = 0.27 mJy beam^{-1}. For both images, the contour levels start at $2\sigma_{\rm rms}$ and are spaced with a factor of $\sqrt{2}$. The $-3\sigma_{\rm rms}$ contours are red, while $2\sigma_{\rm rms}$ contours are dotted green.

to avoid interference on short baseline, i.e., to filter out emission on angular scales larger than 43′. This is a standard procedure used in LoTSS analysis (e.g., Botteon et al. 2022). We performed images at different resolutions: high-resolution (HR) images to subtract point-sources which overlaps to the diffuse emission and low-resolution (LR) images to gain sensitivity to the diffuse emission (see Table 3 for different imaging parameters used in this work).

On the HR image (Fig. 1, left) we identified different sources, named with letters (A, B, C, D), within a radius of 500 kpc (~$0.5R_{500}$) from the cluster center. The emission from these sources contaminates the diffuse emission that we want to study, and thus it has been subtracted. The tailed galaxy on the right, with optical counter part at z = 0.144, is instead quite extended and difficult to remove and disentangle from the diffuse radio emission. Therefore, we decided to not subtract it. The source subtraction is performed directly from the visibilities through a multistep procedure. First, we produced images at high resolution (5″ FWHM) to identify these compact sources (A, B, C, D in Fig. 1, left). We selected the corresponding clean components in the model image and, through an anti-Fourier transform, converted them into visibilities. Finally, a new data set was created as a subtraction of the selected model components' *uv*-data from the original data. Given the slight extension of sources

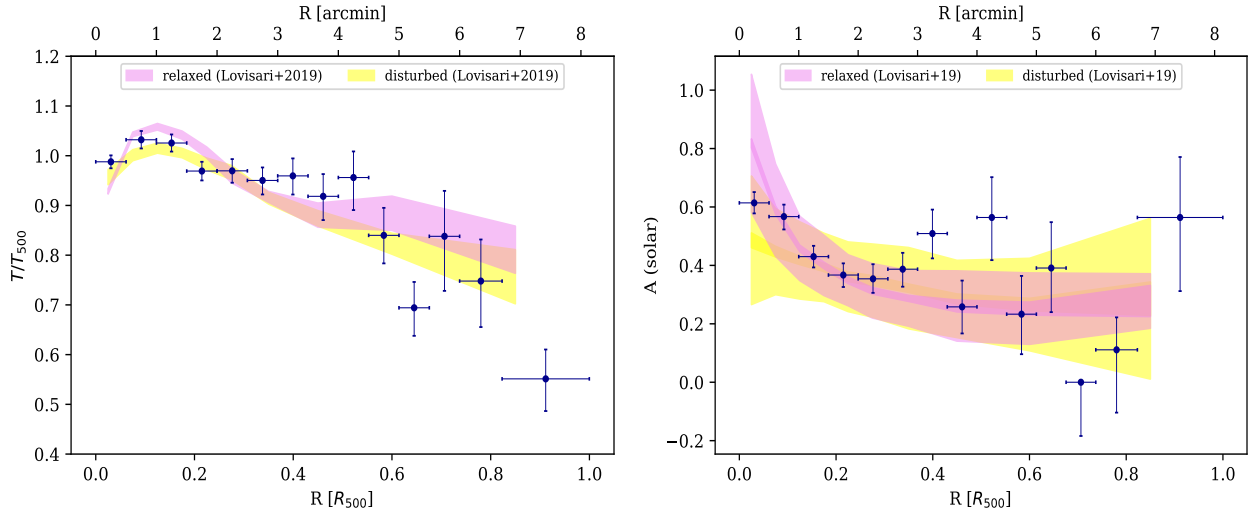

Fig. 2. 1D thermodynamical profiles obtained from spectral fitting, up to R_{500}. Left panel: projected temperature profile. Right panel: metal abundance profile. Both profiles are compared with different averaged values of relaxed system samples (pink) and disturbed ones (yellow) from Lovisari & Reiprich (2019).

A and D, we performed an additional subtraction step, imaging the subtracted data sets at an intermediate ∼10″ resolution. This allowed us to definitively remove all the sources, as they do not leave any residual during inspection of the final *uv*-subtracted data set. Eventually, the final data set is imaged with a negative Briggs weighting with $R = -0.25$ and tapering down the baselines longer than $10\,k\lambda$ (i.e., using a Gaussian taper with a FWHM of 20″) to gain sensitivity on the diffuse emission (see Fig. 1, right).

To ensure a fair comparison with other LOFAR works on the same cluster, we point out that we used different observations respect to the previous LOFAR study of Savini et al. (2019). In particular, these authors used a single 8 h pointed observation, while we combined two pointings for a total of 16 h of observation. Moreover, we used improved calibration techniques that allowed us to produce images with a higher level of sensitivity. For example, our 15″ resolution image has a $\sigma_{\rm rms}$ improved by more than a factor of two with respect to the one of Savini et al. (2019), with $\sigma_{\rm rms} = 450\,\mu$Jy beam at ∼20″-resolution. On the other hand, Riseley et al. (2023) used the same set of observations presented here and achieved comparable sensitivity. However, these authors undertook independent post-processing.

Throughout the paper, the error Δ_S associated with a flux density measurement, S, is estimated as

$$\Delta_S = \sqrt{(\sigma_{\rm c} \cdot S)^2 + N_{\rm beam} \cdot \sigma_{\rm rms}^2}, \quad (1)$$

where $N_{\rm beam} = N_{\rm pixel}/A_{\rm beam}$ is the number of independent beams in the source area, and $\sigma_{\rm c}$ indicates the systematic calibration uncertainty of the flux density, with a typical value of 10% for LOFAR HBA observations (Shimwell et al. 2022). Moreover, we point out that different statistical significance is used, depending on the kind of analysis. In the assessment of the radio diffuse emission's proprieties, such as size, flux density, and power, we employ the standard $3\sigma_{\rm rms}$ detection limit (see Sects. 3.5 and 3.7). This also allows fair comparison with other works on the same cluster (e.g., Govoni et al. 2001; Riseley et al. 2023 cited in the paper). However, as explained in Sect. 4, when performing surface brightness measurements, a $2\sigma_{\rm rms}$ is applied to avoid biased results.

3. Results

As presented in Sect. 1, A1413 is a peculiar galaxy cluster, showing intermediate characteristics between relaxed and merging clusters. Past radio observations have revealed a mini halo at its center (Govoni et al. 2009; Savini et al. 2019). In this section, we present the main results of our X-ray and radio analysis. We used the shape of the surface brightness (SB), temperature, and metallicity profiles, as well as the central cooling time, to determine the cluster's dynamical state. Moreover, we analyzed the radio surface brightness in 1D and 2D to classify the morphology of the radio source and define its properties.

3.1. X-ray azimuthal spectral profiles

The projected temperature profile is shown in Fig. 2 (left). It is well known that for relaxed cool-core galaxy clusters, the temperature profile shows a clear drop in the central region (e.g., Vikhlinin et al. 2005; Pratt et al. 2007). However, for A1413, the temperature does not show the drop in the central region clearly: just the innermost bin (0.5′ ∼ 75 kpc width) shows a drop from 7.43 ± 0.12 to 7.11 ± 0.01 keV. On the other hand, at larger radii the temperature profile decreases as expected for a typical, relaxed cluster. This is consistent with the analysis of Pratt & Arnaud (2002), even if we point out that it could be biased by the low resolution of XMM (as pointed out in Vikhlinin et al. 2005).

We also obtained the metal abundance of the `apec` model, which is a mean abundance gathering the possible emission from different elements (e.g., C, N, O, Ne, Mg, Al, Si, S, Ar, Ca, Fe, Ni), where Fe generally dominates. The profile is displayed in Fig. 2 (right) and does not present clear peak in the cluster core, which is typical of relaxed objects. We compared the observed profiles to average temperature and metallicity profiles for relaxed (pink) and disturbed (yellow) galaxy groups and clusters studied by Lovisari & Reiprich (2019) as a reference. Figure 2 shows that both properties do not clearly follow the mean profile of either relaxed or of disturbed clusters. In the core, where actually relaxed and disturbed cluster profiles differ, A1413 sits in between the two distributions. This supports the scenario that A1413 is an intermediate-phase system.

3.2. X-ray – optical offset

For dynamically relaxed systems, we expect the BCG to be at the center of the gravitational potential well (van den Bosch et al. 2005). Several X-ray studies have proven the correlation between the X-ray peak−BCG offset and the disturbed dynamical state (e.g., Hudson et al. 2010; Mann & Ebeling 2012; Rossetti et al. 2016; Pasini et al. 2021), making this indicator a robust and reliable diagnostic for assessing the dynamical condition of clusters. We find a small offset of about 7.2 kpc between the X-ray peak with the optical BCG. The coordinates of the central galaxy were available RA (J2000) $11^h55^m17^s.87$, Dec (J2000) $+23°24^m16^s.02$ (Rawle et al. 2012) and correspond to the brightest pixel of the optical image, which was retrieved from the HST (*F606W* filter) archive. Despite this offset, recent statistical studies by Rossetti et al. (2016) show that an offset less than $0.02\,R_{500}$ (as in this case 7.2 kpc = $0.006\,R_{500}$) is still consistent with a relaxed system. Moreover, we point out that this offset corresponds to an angular size of ∼3″, which is slightly bigger than the X-ray image's pixel size (∼2″), as used to determine the X-ray peak.

3.3. X-ray surface brightness profile

We computed the radial surface brightness (SB) profiles in the [0.7–2] keV energy band (Fig. 3). This is the energy range where, for temperatures as those observed in A1413, the SB has a very small dependence on the kT and it also provides an optimal ratio of the source and background flux in *XMM-Newton* data. The annuli for the SB profile are again centered on the X-ray peak and have been determined by requiring a fixed $S/N = 10$ and minimum width of 2″.

The profile is fit with a double β-model (LaRoque et al. 2006) in the following form:

$$\Sigma = \Sigma_{01}\left[1+\left(\frac{r}{r_{c1}}\right)^2\right]^{-3\beta_1+1/2} + \Sigma_{02}\left[1+\left(\frac{r}{r_{c2}}\right)^2\right]^{-3\beta_2+1/2}, \quad (2)$$

where r_{c1},r_{c2} are the core radii, Σ_{01}, Σ_{02} are the central surface brightnesses of the two components, and β represents the ratio of specific kinetic energies of galaxies and gas (e.g., Gitti et al. 2012). This is the extension of the isothermal β model (Cavaliere & Fusco-Femiano 1976), commonly used to describe the surface brightness profile of the ICM. In fact, when fitting the profile over the radial range with a single β model, we found the presence of a central excess. This biases the best-fit results toward a small core radius and overestimates the true profiles in the region outside the excess ($r \gg r_c$), producing non-random strong residuals. Thus, a second component was needed and is typically required to reproduce the sharp X-ray peak in the core of relaxed clusters (e.g., Mohr et al. 1999; Pratt & Arnaud 2002; Pasini et al. 2019).

3.4. Cooling time

From the temperature and density profiles, the cooling time of each region can be estimated as

$$t_{cool} = \frac{H}{\Lambda(T) n_e n_p} = \frac{\gamma}{\gamma-1}\frac{kT(r)}{\mu X n_e(r)\Lambda(T)}, \quad (3)$$

where $\gamma = 5/3$ is the adiabatic index, H is the enthalpy, $\mu \sim 0.6$ is the molecular weight for a fully ionised plasma, and $\Lambda(T)$ is the cooling function (Sutherland & Dopita 1993). Given the cooling profile, we can define the cooling radius, i.e., the radius

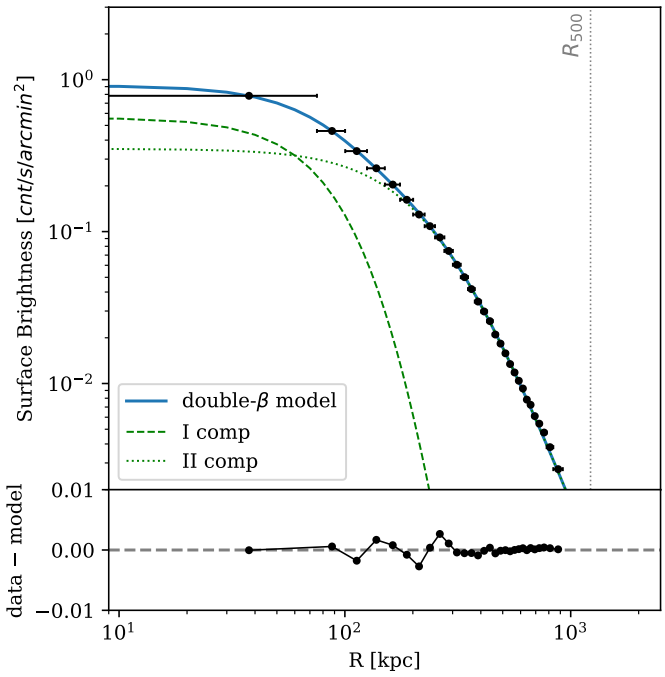

Fig. 3. X-ray surface brightness profile, together with the best-fit double-β model of Eq. (2). The best-fit parameters are $\Sigma_{01} = 0.56 \pm 0.05$ cst s^{-1} arcmin^{-2}, $r_{c1} = 189.62 \pm 0.41$ kpc, $\beta_1 = 2.17 \pm 0.91$ and $\Sigma_{02} = 0.35 \pm 0.04$ cst s^{-1} arcmin^{-2}, $r_{c2} = 257.04 \pm 0.25$ kpc, $\beta_2 = 0.80 \pm 0.04$ with χ^2/d.o.f. ≃ 1.64. The vertical line indicates R_{500}. The surface brightness values have errors on the order of 1–2%; thus, error bars on the y-axis are not visible in this plot.

at which the cooling time is less than the age of the system. The latter can be estimated assuming the cluster's age to be equal to the look-back time at $z = 1$, that is, $t_{age} \simeq 7.7$ Gyr (e.g., Bîrzan et al. 2004; Gitti et al. 2012), as at this time many clusters appear to be relaxed (Fig. 4, red line). To obtain r_{cool}, we qualitatively fit the cooling-time profile with a power-law relation and selected r_{cool} as the intersection between the best-fitting power law and t_{age}. Thus, the cooling region for A1413 is within $r_{cool} = 0.6$ arcmin = 90 kpc (Fig. 4, green vertical line).

Hudson et al. (2010) argued that the central cooling time t_{cool} is the best parameter for low-redshift clusters to identify cool-core and non-cool-core clusters. They divided clusters into three types: $t_{cool} < 1$ Gyr for strong cool-core clusters; $t_{cool} \sim 1-7.7$ Gyr for weak cool-core clusters; $t_{cool} > 7.7$ Gyr for non-cool-core clusters. Following the definition of a cool core based on the cooling time given by Hudson et al. (2010), A1413 appears to be a weak cool-core cluster with a central cooling time of $t_{cool} = 6.4 \pm 1.3$ Gyr within $r < 0.5' \sim 75$ kpc.

3.5. Radio morphology

Previous studies of A1413 at 1.4 GHz (Govoni et al. 2009) and 144 MHz (Savini et al. 2019) frequencies confirmed the cluster is hosting a central mini halo. Thanks to the improved calibration strategy and our deeper LOFAR HBA observations, we detect low-surface-brightness emission that extends further out from the cooling region, only visible in the LoTSS images. It is elongated in the north-south direction, as happens for the X-ray, and has a maximum linear size of $D \sim 800$ kpc ($3\sigma_{rms}$-contour), on scales typical of giant radio halos (see source-subtracted

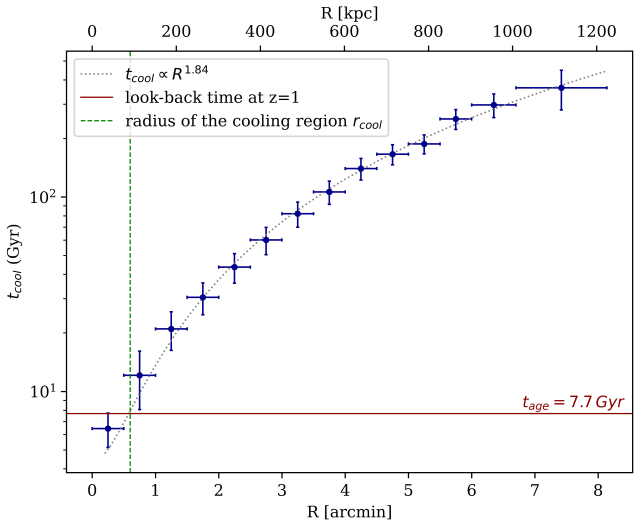

Fig. 4. Cooling time profile for A1413. The red solid line represents the look-back time at $z = 1$, $t_{age} = 7.7$ Gyr. The power-law fit with $t_{cool} = 9.27R^{1.84}$ allows us to define the cooling radius (green vertical line), namely the region within which $t_{cool} < t_{age}$.

35″-resolution image of Fig. 1, right). West of the cluster, a head-tail radio galaxy with optical counterpart at $z = 0.144$ (i.e., consistent with the cluster's redshift) is present, which appears to be connected with the outer radio emission, though we cannot exclude projection effects. Given the new discovery, we analysed the radio emission of the cluster to understand whether we detected a giant radio halo or the superposition of two different sources (mini halo plus halo emission), as was recently found in a few other clusters (RX J1720.1+2638 of Biava et al. 2021, Abell 2142 of Bruno et al. 2023a).

3.6. Radio surface-brightness profiles

The exponential profile has been customarily used to fit the SB profile of giant and mini halos (e.g., Murgia et al. 2009; Botteon et al. 2022; Bonafede et al. 2022; Cuciti et al. 2022). This is a simple model with only two free parameters, and it provides a reasonable description of many radio halos. We studied the radio surface brightness, making use of two approaches: we first performed a 1D analysis following the fitting procedure of Murgia et al. (2009), and then we used the more recent 2D method developed by Boxelaar et al. (2021).

However, we point out that this is not a physical model, and Botteon et al. (2022, 2023) showed that the exponential one is not always a good model for representing halos. In particular, when halos present substructures in the radio emission (such as edges and filaments), the exponential smooth profile leaves strong residuals.

Following Murgia et al. (2009), we calculated the radio brightness profile, averaged in concentric annuli of 15″ in width, i.e., the FWHM of an image beam, centered on the peak of the radio halo (Fig. 5). In fact, to increase the number of points for the fit, we used the source-subtracted 15″ resolution image, which is the most sensitive to the central mini-halo emission. To test the double morphology of the radio source, we extended the procedure of Murgia et al. (2009) using a double exponential law of the form

$$I(r) = I_{0,1}e^{-r/r_{e,1}} + I_{0,2}e^{-r/r_{e,2}}, \quad (4)$$

where the parameters are the central radio surface brightnesses $I_{0,1}, I_{0,2}$ and the corresponding e-folding radii $r_{e,1}, r_{e,2}$, the length scales at which the surface brightness drops to I_0/e. We masked all the discrete sources in the cluster outskirts that would possibly overlap with the extended emission (red regions of Fig. 5, left) and stopped the profile where average surface brightness is two times the detection limit in each annulus $\sigma_{\rm annulus} = \sigma_{\rm rms}/\sqrt{N_{\rm beam}}$ (dashed black line in Fig. 5, left), which corresponds to $0.4R_{500}$ from the cluster center. The resulting profile is shown in Fig. 5 (right) and the best-fit parameters are listed in Table 4. We see clear evidence of an inner brighter component and a second broader emission, with a surface brightness being one order of magnitude lower than that of the inner one. This double-exponential fit allows us to set a boundary on the extension of the inner component. Motivated by the empirical evidence that halos do not extend indefinitely, it is customary to adopt a source radius of $3r_e$ (Murgia et al. 2009; Botteon et al. 2022; Bruno et al. 2023b), which contains 80% of the flux that would be obtained when integrating the model up to infinity $S_\nu(< 3r_e) = 0.8S_\nu^\infty$. Thus, we fixed the size of the mini halo to three times the e-folding radius of the first model component, $R = 3r_{e,1} = 84$ kpc. The second component results to have a extension of $R_{\rm ext} = 3r_{e,2} = 870$ kpc, which corresponds to a total size of $D_{\rm ext} \sim 1.7$ Mpc. This means double the size based on the $3\sigma_{\rm rms}$ contours of Sect. 3.5. We notice that the fit e-folding radius for the inner component is smaller that the value of Riseley et al. (2023), who measured a total extent of 343 kpc (i.e., a radius of ∼170 kpc) at 144 MHz, using the same LOFAR observations. However, we point out that those authors focus their study on the inner component only, using a higher $3\sigma_{\rm rms}$ threshold and more robustly weighted imaging parameters for a better spatially resolved spectral analysis. When using common imaging settings, the results are consistent. We also notice the presence of several $2\sigma_{\rm rms}$ contours with filamentary morphology around the central mini halo of Fig. 5 (left), which we attribute to the extended halo component. To exclude the possibility of chance occurrences, we analysed the surface brightness profiles of several other radio sources within the same field of view. This examination revealed the absence of plateau-like features similar to that depicted in Fig. 5 (right), confirming its association with the extended radio component.

We then analyzed the low-resolution (35″ × 35″) image, where the broader extended emission can be detected at a higher signal-to-noise ratio (Fig. 1, right) using a Halo-Flux Density CAlculator[8] (HALO-FDCA, Boxelaar et al. 2021) fitting procedure. This method fits the surface brightness profile of halos to a 2D model using Bayesian inference and allows us to extend the exponential 1D model, taking into account different shapes of halos (circular, elliptical, or skewed). Moreover, it is able to perform flux density and size estimations that are less affected by the image noise. The general exponential model used by Boxelaar et al. (2021) is

$$I(\boldsymbol{r}) = I_0 e^{-G(\boldsymbol{r})}, \quad (5)$$

where I_0 is the central surface brightness value and $G(\boldsymbol{r})$ the function that takes different forms depending on the complexity of the model. In the circular model case, $G(\boldsymbol{r}) = |\boldsymbol{r}|/r_e$ recalls the exact 2D version of the exponential profile used in Murgia et al. (2009). Since HALO-FDCA is not built for a double-component emission, we additionally masked the central mini halo region to derive flux coming from the extended emission only (Fig. A.1). In masked regions, HALO-FDCA performs an extrapolation of

[8] https://github.com/JortBox/Halo-FDCA

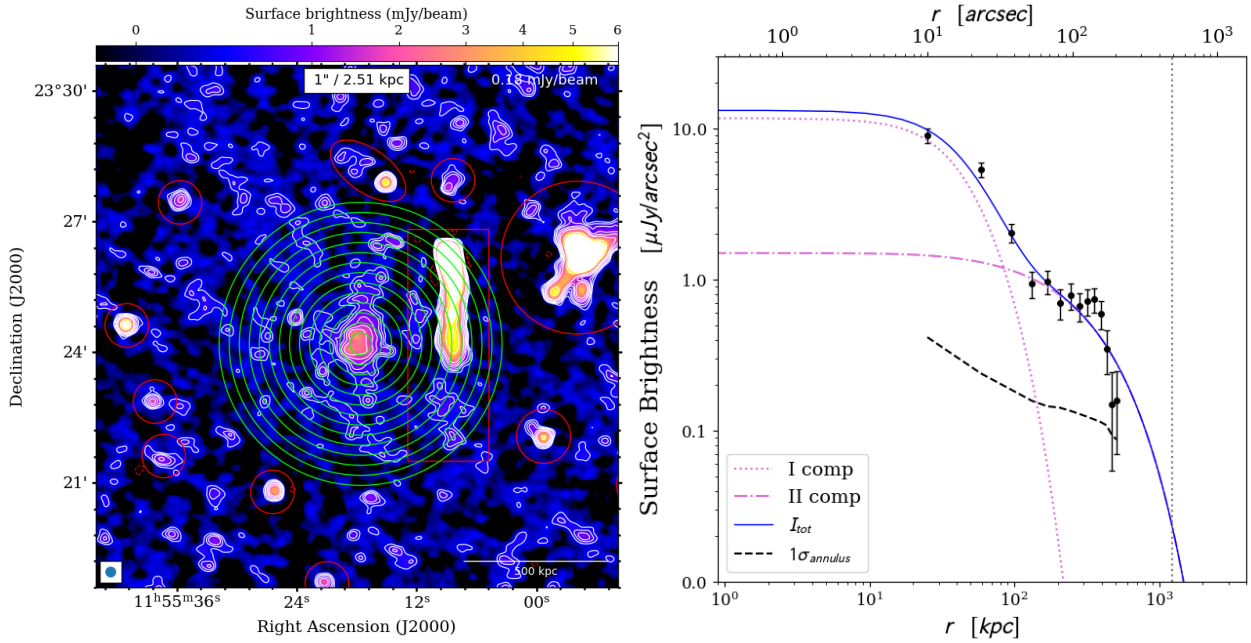

Fig. 5. 1D radio surface-brightness profile. Left panel: medium resolution ($15'' \times 15''$) source-subtracted image at 144 MHz. Masked regions are shown in red, together with the green annuli where the surface brightness has been extracted. The contour levels start at $2\sigma_{\rm rms}$, where $\sigma_{\rm rms} = 0.18\,{\rm mJy\,beam^{-1}}$, and are spaced with a factor of $\sqrt{2}$. The $-3\sigma_{\rm rms}$ contours are red. Right panel: radio surface-brightness profile. The solid line represents the resulting double exponential model, while the single components are plotted as a reference. The central mini-halo component has $r_{e,1} = 28 \pm 5$ kpc, while the second broader component has $r_{e,2} = 290 \pm 60$ kpc. The vertical line indicates R_{500}, and the dashed black line indicates the $1\sigma_{\rm annulus}$ detection limit for each annulus.

Table 4. Summary of main properties of radio emission in A1413.

	ν MHz	D kpc	$S_{3\sigma}$ mJy	$P_{3\sigma}$ W Hz^{-1}	$I_{0,12}$ μJy arcsec^2	$r_{e,12}$ kpc	χ
Halo	144	(800, 500)	37 ± 6	$1.9 \pm 0.3\,10^{24}$	1.6 ± 0.4	290 ± 60	1.8
Mini-Halo	144	$220^{(\star)}$	23 ± 2	$(1.2 \pm 0.1) \times 10^{24}$	23 ± 5	28 ± 5	
	1440	220	1.9 ± 0.7	$(1.0 \pm 0.1) \times 10^{23}$			

Notes. Column 1: Name of the radio source; Col. 2: Size measured above $3\sigma_{\rm rms}$ contour. For the halo, the two measures refer to ($D_{\rm max}$, $D_{\rm min}$) in the north-south and west-east directions, respectively. Listed result at 1440 MHz from Govoni et al. (2009). $^{(\star)}$Since in LOFAR observations it is impossible to disentangle the mini halo, we used the 220 kpc region as a reference (see Sect. 3.7). Column 3: Flux density measured within the $3\sigma_{\rm rms}$ contour; Col. 4: Radio power with the k correction applied, assuming $\alpha = -1.2$; Col. 5: Central surface brightness of the double-exponential profile of Eq. (4); Col. 6: e-folding radius of the double-exponential profile of Eq. (4); Col. 7: reduced χ^2 of the fit.

the model. The masked circular mini halo region has a size of $R = 84$ kpc based on the 1D fitting results. Despite the clear elliptical shape of the extended radio emission, elongated in the north-south direction (Fig. 1, right), HALO-FDCA does not find the elliptical model to be a better representation of the source (see Figs. A.1 and 5). From the circular 2D model, we obtain the e-folding radius $r_e^{\rm FDCA} = 224 \pm 16$ kpc (i.e., $R_{\rm ext}^{\rm FDCA} = 3r_e^{\rm FDCA} \sim 675$ kpc, which corresponds to $D_{\rm ext}^{\rm FDCA} \sim 1.3$ Mpc) and a flux of $S^{\rm FDCA} = 106 \pm 8$ mJy integrated until $3r_e^{\rm FDCA}$. The best-fit results are listed in Table 5.

The two fitting methods give compatible results for the extended component: $r_{e,2} = 290 \pm 60$ kpc and $r_e^{\rm FDCA} = 224 \pm 16$ kpc, for the 1D and HALO-FDCA e-folding radius, respectively. Moreover, both methods find the second component to be wider compared to the 800 kpc size based on the $3\sigma_{\rm rms}$ contour of Fig. 1, with a total linear size of $D_{\rm ext} > 1.2$ Mpc. This suggests the presence of a second, very-low-surface-brightness radio emission filling the cluster volume, overlapped with the previously known central mini halo.

3.7. Mini halo integrated spectral index

The radio mini halo emission detected by Govoni et al. (2009; Fig. 6) is about $1.5'$ ($\simeq$220 kpc) in size and has a flux density of $S_{1.4\,\rm GHz} = 1.9 \pm 0.7$ mJy, which corresponds to a power of $P_{1.4\,\rm GHz} = 1.0 \times 10^{23}\,{\rm W\,Hz^{-1}}$ (see Table 4). We caution that this flux-density value should be considered as an upper limit to the actual flux density of the mini halo at 1.5 GHz. Indeed, just the contribution from a single unresolved source (source A in our analysis) detected in the FIRST survey (Becker et al. 1995) was considered, whereas an additional point source is embedded within the mini halo, as shown by our LOFAR high-resolution image (Sect. 1, left, source B). To estimate the integrated spectral index of the mini halo emission, we re-imaged the LOFAR data at the same $15'' \times 15''$ resolution and with the common inner uv-cut of 180λ, minimum baseline of VLA image. To be consistent with Govoni et al. (2009), we used a circular region with $r \sim 0.7' \sim 110$ kpc and find a total flux density of $S_{144\,\rm MHz} = 23 \pm 2$ mJy (Table 4). The integrated spectral

Table 5. Summary of HALO-FDCA results for extended emission in A1413.

	ν MHz	I_0 μJy arcsec^{-2}	$r_{e,1}$ kpc	$r_{e,2}$ kpc	$r_{e,3}$ kpc	$r_{e,4}$ kpc	$S_{<3r_e}$ mJy	$P_{<3r_e}$ W Hz^{-1}	χ	Model	Ref.
Halo	144	2.6 ± 0.2	224 ± 16	–	–	–	106 ± 8	$(6.0 \pm 0.5) \times 10^{24}$	0.823	Circle	Fig. A.1 (top panel)
		2.6 ± 0.2	228 ± 17	224 ± 16	–	–	107 ± 8	$(6.0 \pm 0.5) \times 10^{24}$	0.828	Ellipse	Fig. A.1 (middle panel)
		2.6 ± 0.2	295 ± 40	227 ± 35	148 ± 25	255 ± 34	109 ± 8	$(6.0 \pm 0.5) \times 10^{24}$	0.769	Skewed	Fig. A.1 (bottom panel)

Notes. Column 1: Name of the radio source; Col. 2: Frequency; Col. 3: Central surface brightness obtained by HALO-FDCA, Eq. (5); Col. 4: e-folding radius obtained by HALO-FDCA (circular model); Col. 5: (elliptical model); Col. 6: (skewed model); Col. 7: Flux density measured by HALO-FDCA the $3r_e$; Col. 8: Radio power with the k correction applied, assuming $\alpha = -1.2$; Col. 9: Reduced χ^2; Col. 10: Reference image.

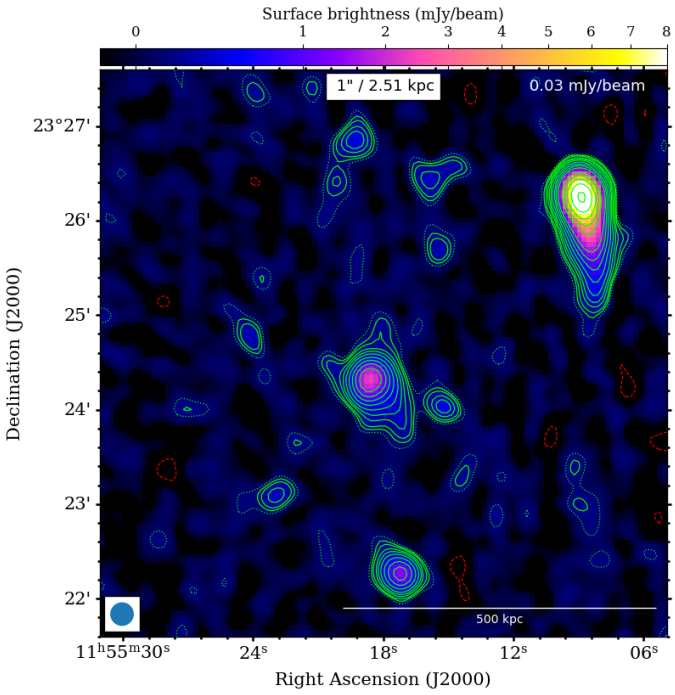

Fig. 6. Radio image at 1.5 GHz with beam of 15″×15″. The contour levels start at $2\sigma_{\rm rms}$, where $\sigma_{\rm rms} = 0.035$ mJy beam^{-1}, and they are spaced with a factor of $\sqrt{2}$. The $-3\sigma_{\rm rms}$ contours are red, while $2\sigma_{\rm rms}$ contours are dotted green. This image, shown here to provide context, is derived from and presented in Govoni et al. (2009).

index between 144 MHz and 1.5 GHz is $\alpha = 1.1 \pm 0.2$. We note that the spectral index might be steeper, considering that the flux reported by Govoni et al. (2009) could be slightly overestimated, as explained above.

As the extended halo emission is not detected in the VLA image, we tried to put a lower limit on its average spectral index, comparing the mean surface brightness of the extended emission at 144 MHz with the rms noise of VLA image. To do this, we considered a rectangular area that follows the $3\sigma_{\rm rms}$ contours of the 800 kpc scale emission (Fig. 1, right) and excluded the central $r < 0.7'$. Unfortunately, this does not allow us to firmly constrain the spectral index of the external emission, as we find $\alpha > 0.75$ at $1\sigma_{\rm rms}$. Riseley et al. (2023) produced resolved spectral map combining MeerKAT at 1283 MHz with LOFAR at 145 MHz data and found that the innermost region ($R \lesssim 50$ kpc, which corresponds to $\sim 2r_{e,1}$ of our inner component) shows a flatter spectral index around -0.7 to -1, while there is a hint of larger scale diffuse emission with a typical spectral index of around -1.1 or steeper. The different spectral index of the two regions may suggest the presence of two different types of radio emission co-existing in the same cluster. Further investigation about the hybrid morphology of the radio emission is performed in Sect. 4, where X-ray properties are also considered.

4. Discussion: Spatial correlation between X-ray and radio surface brightness

Quantitative studies to investigate the point-to-point correlation between the radio and X-ray brightness distribution of giant halos can provide useful information about the connection between the thermal and nonthermal emission (e.g., Govoni et al. 2001; Feretti et al. 2001; Giacintucci et al. 2005). However, most of the literature studies were limited by the resolution and sensitivity of the radio and X-ray observations. Now, thanks to deep and sensitive observations, these studies can be carried out in more detail and also extend the sample to mini halos (Ignesti et al. 2020; Botteon et al. 2020; Rajpurohit et al. 2021; Biava et al. 2021; Duchesne et al. 2021; Bonafede et al. 2022; Riseley et al. 2022a,b). These recent studies have shown different trends for giant and mini halos. Halos show a linear or sublinear scaling, while mini halos tend to have a superlinear one.

The correlation is generally investigated via a power-law relationship of the following kind:

$$\log I_R = A \log I_X + B, \tag{6}$$

where the slope of the scaling A determines whether the radio brightness (i.e., the magnetic field strength and CRe density) declines faster ($A > 1$) than the X-ray brightness (i.e., the thermal gas density), or vice versa ($A < 1$). The connection between thermal and nonthermal plasma could reflect the particle reacceleration mechanism, and it could be used to discriminate between models of halo formation (Govoni et al. 2001).

To compute these correlations, we used the `LinMix`[9] package (Kelly 2007), which uses a Bayesian approach to linear regression and allows us to consider measurement uncertainties on both quantities. The threshold for upper limits is fixed at $2\sigma_{\rm rms}$ in the radio image following Botteon et al. (2020). These authors noted that the introduction of a high threshold combined with a large intrinsic scatter can introduce a bias in the correlation and demonstrated that a threshold of $2\sigma_{\rm rms}$ is the right choice. The strength of the correlation is measured by the Pearson $r_{\rm p}$ and Spearmann $r_{\rm s}$ correlation coefficients. The former assesses the linear relation between the two variables, while the latter determines their monotonic relation (whether linear or not).

Based on the two-component emission found with the surface brightness analysis of Sect. 3.6, we performed point-to-point correlation separately for both the extended and mini-halo emission, using the radio images at 144 MHz presented in Figs. 1

[9] https://linmix.readthedocs.io/en/latest/index.html

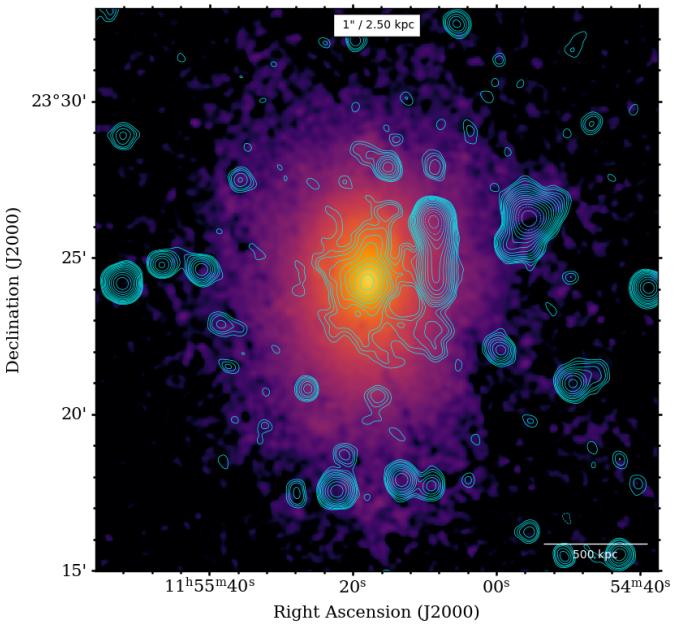

Fig. 7. Background-subtracted and exposure-corrected *XMM-Newton* image of A1413 in [0.7–2] keV energy band. Radio contours from 35″ LOFAR HBA image at 144 MHz Fig. 1 (right) are over-plotted.

Table 6. `LinMix` best-fit parameter for I_R–I_X correlation of Fig. 8.

Region	Grid	A	r_p	r_s	Ref.
Halo	$35'' \times 35''$	$0.81^{+0.07}_{-0.08}$	0.87	0.85	Fig. 8 (left)
	$35'' \times 35''$	$0.78^{+0.08}_{-0.07}$	0.83	0.82	Fig. 8 (left)
Mini-halo	$23'' \times 23''$	$1.27^{+0.16}_{-0.14}$	0.93	0.91	Fig. 8 (right)

Notes. Column 1: Considered radio source; Col. 2: Grid box size; Col. 3: Fitting slopes (A); Col. 4: Pearson (r_p), and Col. 5: Spearmann (r_s) correlation coefficients; Col. 6: Reference plot.

(right) and Fig. 5 (left) together with the *XMM-Newton* images presented in Fig. 7. Following Govoni et al. (2001), we constructed a grid covering the cluster region and calculated, for each box, the mean radio and X-ray quantities, as well as the rms, which can be assumed as an estimate of the statistical error. The size of the boxes was chosen to be equal to 1.5 times the area of the radio beam (see Table 6). This grid resolution also allows it to be minimally affected by the PSF of *XMM-Newton*, which for the combined MOS+pn images is ∼10″ (FWHM).

First, we performed the correlation on the 35″-resolution image (Fig. 1, right) to study the properties of the extended emission. The total considered area was chosen based on the lowest X-ray brightness level, which includes the radio emission and excludes other external radio sources, in order to select a homogeneous and not radio-biased area. Both point-like and extended (the tailed galaxy) contaminating sources in the radio image were identified, and cells containing them were removed. Presumably, the tailed galaxy also influences some contiguous regions south of the tail; thus, a safe choice is to exclude these regions too. Final selections (blue boxes) and upper limits (cyan boxes) are shown in the top left corner of each plot of Fig. 8.

The two surface brightnesses are positively correlated $r_p = 0.87, r_s = 0.85$ and have a sublinear scaling $A = 0.81^{+0.07}_{-0.08}$. This is in agreement with other literature works for giant halos (e.g., Botteon et al. 2020; Rajpurohit et al. 2021; Riseley et al. 2022a). We notice four points, spatially corresponding to the central brighter component, that appear distinctly separated from the extended component ones on the correlation. To exclude that those points are biasing the correlation toward steeper values, we performed it again, removing these four central boxes. This also allowed us to study the correlation properties of the outer component only. We still find a sublinear ($A = 0.78^{+0.08}_{-0.07}$)) strong ($r_p = 0.83, r_s = 0.82$) correlation consistent with the previous one. The absence of statistical difference between the two results confirms that the correlation is determined by the extended emission and reinforces the robustness of our initial findings.

The correlation indicates that the decline of the nonthermal radio component is shallower than the thermal one. This slope can be explained by re-acceleration models, while it is a challenge for hadronic models (as explained by Govoni et al. 2001).

We then studied the central mini-halo component, making use of the higher 15″-resolution radio image (Fig. 5), which is the most sensitive to the central emission and allows us to better sample the inner region. Differently from the sublinear or linear scalings that are reported in the literature for giant radio halos, but consistently with the sample of mini halos studied by Ignesti et al. (2020), we find instead a superlinear $A = 1.27^{+0.16}_{-0.14}$ correlation for the central emission (Fig. 8, right). Also in this case, there is clear evidence of a spatial correlation between radio and X-ray emission, with $r_p = 0.93, r_s = 0.91$ (Table 6). This superlinear correlation is also consistent with analysis of Riseley et al. (2023), who found $A = 1.20^{+0.13}_{-0.11}$ using LOFAR data at 144 MHz and $A = 1.63^{+0.10}_{-0.10}$ reproducing the correlation with MeerKAT data at 1283 MHz. The superlinear scaling between I_R and I_X suggests that the number density of emitting electrons and magnetic field rapidly declines from the center to the external regions. In particular, the radio emission is more peaked than the thermal emission, indicating that the ICM nonthermal component is more concentrated around the central AGN. This is consistent with the hadronic scenario that predicts a superlinear scaling between the surface brightness for a radially decreasing magnetic field (e.g., Govoni et al. 2001). We note, however, that the re-acceleration model cannot be excluded. Depending on the CRe distribution, it could also produce a superlinear scaling of the X-ray and radio surface brightnesses.

The different trends of the two radio sources further strengthen the idea that the radio emission of A1413 is composed of two different components. They might also mean that the mechanisms responsible for the re-acceleration of the radio-emitting particle are different.

5. Conclusions

In this work, we present a composite X-ray and radio analysis of the galaxy cluster A1413. For this purpose, *XMM-Newton* and LOFAR 144 MHz data were first analyzed separately. They were then combined to quantify the connection between the thermal and nonthermal components of the ICM. The main results can be summarized as follows.

1. The X-ray morphology of the cluster on large scales is not spherically symmetric, confirming the ellipticity found in previous work in both optical and X-ray bands. This morphology suggests the occurrence of a merger that has left a clear, though minor, imprint on the gas distribution along the N–S axis of the cluster. Other dynamical features indicate that A1413 is an intermediate-phase cluster: The temperature profile in the core does not decline sharply as is expected in the inner regions of a strong cool-core

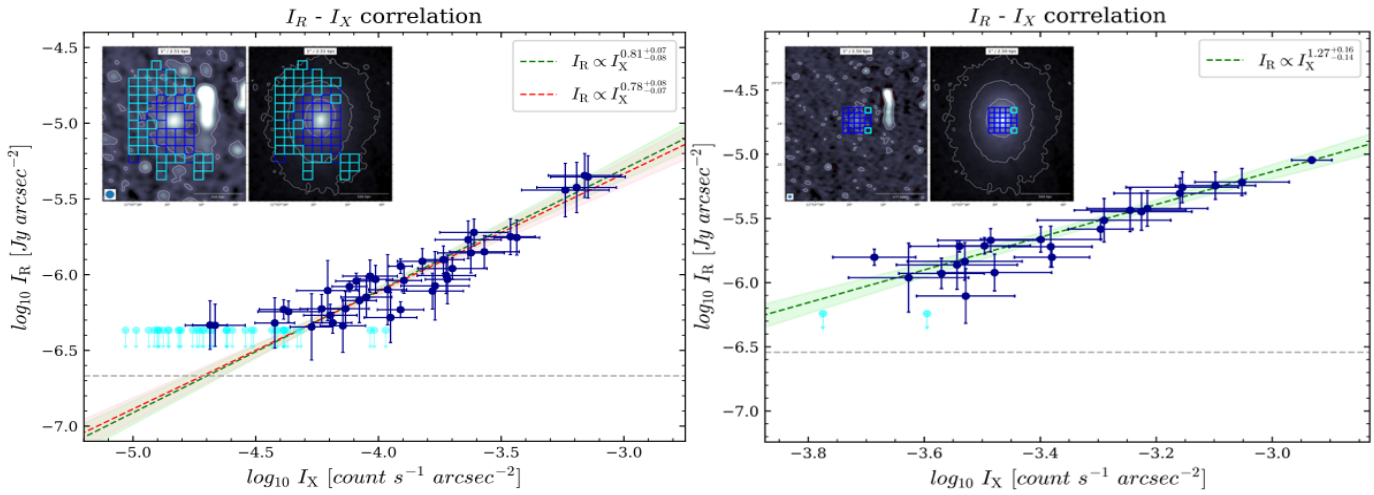

Fig. 8. Spatial correlation between X-ray and radio surface brightness. Left panel: I_R–I_X relation of the halo in A1413, extracted in square boxes with width of 35″. The horizontal gray dash-dotted lines indicate the $\sigma_{\rm rms} = 298\,\mu$Jy beam^{-1} in the radio maps. Right panel: $I_R - I_X$ relation of the mini halo in A1413, extracted in square boxes with a width of 23″. The horizontal gray dash-dotted lines indicate the $\sigma_{\rm rms} = 203\,\mu$Jy beam^{-1} in the radio maps. For both relations, upper limits (cyan points) refer to cells where the radio surface brightness is below the $2\sigma_{\rm rms}$ level. The best-fit (green dashed line) is reported with the corresponding 1σ confidence interval. Red dashed best-fit line (left panel) refers to the correlation without the four central boxes.

cluster. Moreover, the metallicity profile is flatter than expected for a very relaxed system. However, the surface brightness profile is well fit with a double β model, which typically accounts for the central brightness excess of cool-core clusters. Finally, from the calculation of the cooling time, we obtain $t_{\rm cool} = 6.4 \pm 1.3$ Gyr within $r < 0.5' \sim 75$ kpc, and a cooling region of $r_{\rm cool} \sim 90$ kpc. We argue that such a system with a moderate cooling time, an elevated central entropy, and a slightly decreasing central temperature profile can be classified as a weak cool-core system (Hudson et al. 2010).

2. A1413 was known to host a mini-halo (Govoni et al. 2009; Giacintucci et al. 2017; Savini et al. 2019; Riseley et al. 2023). The LOFAR HBA data at 144 MHz led to the discovery of an extended, low-surface-brightness emission, with an LLS of about 800 kpc in the N–S direction based on the $3\sigma_{\rm rms}$-contours, so far detected only at low frequencies. To date, this is one of the few objects that show a wider emission surrounding a previously known central mini halo and with a size typical of giant radio halos.
3. We performed 1D surface brightness fitting using the double exponential model of Eq. (4). We find an inner brighter component extended up to $R = 84$ kpc, which is consistent with other mini halos, and a broader component with $R_{\rm ext} = 870$ kpc. Additionally, we performed a 2D fitting of the extended component only using the HALO-FDCA software. To do that, we masked the internal region, and we obtained best-fit values of $R_{\rm ext}^{\rm FDCA} = 3r_e^{\rm FDCA} \sim 675$ kpc for the circular model (see Table 5). Both methods give consistent results and find the second component to be wider than the 800 kpc size based on the $3\sigma_{\rm rms}$ contour of Fig. 1, with a total linear size of $D_{\rm ext} > 1.2$ Mpc.
4. We performed a point-to-point correlation analysis between the X-ray and radio surface brightness, which confirms the spatial connection between the nonthermal and thermal emission in galaxy clusters. We investigated a possible correlation for both the halo and the mini-halo regions separately. We found a sublinear correlation $I_R \propto I_X^{0.78^{+0.08}_{-0.07}}$ when analyzing the extended part and a superlinear $I_R \propto I_X^{1.27^{+0.16}_{-0.14}}$ correlation for the inner mini-halo component. Sublinear or linear scalings are reported in the literature for giant radio halos and can be explained by the re-acceleration scenario. On the other hand, superlinear correlations are usually found for minihalos, indicating that the ICM nonthermal component is more concentrated around the central AGN. This is consistent with the hadronic scenario. Nevertheless, the re-acceleration model cannot be excluded, as depending on the CRe distribution, it could also produce a superlinear scaling.

The properties of this cluster show all the signs of an intermediate-state cluster, dynamically not fully relaxed and with diffuse radio emission outside the central cooling region, as would be expected for cool-core objects. Both the SB fitting and the I_R–I_X correlations confirm the presence of two components as found in other clusters with the same dynamical characteristics (e.g., RX J1720.1+2638, Biava et al. 2021; A2142, Bruno et al. 2023a). The mini halo and the diffuse emission extend over different scales and show different features, suggesting that the mechanisms responsible for the re-acceleration of the radio-emitting particles are different. The outer component might probe turbulent re-acceleration induced by less energetic merger events. In this context, we argue that minor merger events can induce particle acceleration on large scales without fully disrupting the cluster core. Considering its hybrid radio morphology and intermediate X-ray properties, A1413 is a peculiar object that challenges the long-lasting picture of disturbed galaxy clusters hosting giant radio halos and relaxed ones with mini halos.

Acknowledgements. This research project made use of the following Python packages: APLpy (Robitaille & Bressert 2012), Astropy (Astropy Collaboration 2013) and NumPy (van der Walt et al. 2011). C.J.R. and A. Bonafede acknowledge financial support from the ERC Starting Grant 'DRANOEL', number 714245. LL acknowledges financial contribution from the INAF grant 1.05.12.04.01. M.B. acknowledges support from the Deutsche Forschungsgemeinschaft under Germany's Excellence Strategy – EXC 2121 "Quantum Universe" – 390833306 and from the BMBF ErUM-Pro grant 05A2023. R.J.v.W. acknowledges support from the ERC Starting Grant ClusterWeb 804208.

A. Botteon acknowledges financial support from the European Union – Next Generation EU. LOFAR (van Haarlem et al. 2013) is the Low Frequency Array designed and constructed by ASTRON. It has observing, data processing, and data storage facilities in several countries, which are owned by various parties (each with their own funding sources), and that are collectively operated by the ILT foundation under a joint scientific policy. The ILT resources have benefited from the following recent major funding sources: CNRS-INSU, Observatoire de Paris and Université d'Orléans, France; BMBF, MIWF-NRW, MPG, Germany; Science Foundation Ireland (SFI), Department of Business, Enterprise and Innovation (DBEI), Ireland; NWO, The Netherlands; The Science and Technology Facilities Council, UK; Ministry of Science and Higher Education, Poland; The Istituto Nazionale di Astrofisica (INAF), Italy. This research made use of the Dutch national e-infrastructure with support of the SURF Cooperative (e-infra 180169) and the LOFAR e-infra group. The Jülich LOFAR Long Term Archive and the German LOFAR network are both coordinated and operated by the Jülich Supercomputing Centre (JSC), and computing resources on the supercomputer JUWELS at JSC were provided by the Gauss Centre for Supercomputing e.V. (grant CHTB00) through the John von Neumann Institute for Computing (NIC). This research made use of the University of Hertfordshire high-performance computing facility and the LOFAR-UK computing facility located at the University of Hertfordshire and supported by STFC [ST/P000096/1], and of the Italian LOFAR IT computing infrastructure supported and operated by INAF, and by the Physics Department of Turin university (under an agreement with Consorzio Interuniversitario per la Fisica Spaziale) at the C3S Supercomputing Centre, Italy.

References

Arnaud, K. A. 1996, ASP Conf. Ser., 101, 17
Astropy Collaboration (Robitaille, T. P., et al.) 2013, A&A, 558, A33
Bade, N., Engels, D., Voges, W., et al. 1998, A&AS, 127, 145
Baldi, A., Ettori, S., Mazzotta, P., Tozzi, P., & Borgani, S. 2007, ApJ, 666, 835
Becker, R. H., White, R. L., & Helfand, D. J. 1995, ApJ, 450, 559
Biava, N., de Gasperin, F., Bonafede, A., et al. 2021, MNRAS, 508, 3995
Bîrzan, L., Rafferty, D. A., McNamara, B. R., Wise, M. W., & Nulsen, P. E. J. 2004, ApJ, 607, 800
Böhringer, H., Voges, W., Huchra, J. P., et al. 2000, ApJS, 129, 435
Bonafede, A., Intema, H. T., Bruggen, M., et al. 2014, MNRAS, 444, L44
Bonafede, A., Brunetti, G., Rudnick, L., et al. 2022, ApJ, 933, 218
Botteon, A., Gastaldello, F., & Brunetti, G. 2018, MNRAS, 476, 5591
Botteon, A., Brunetti, G., van Weeren, R. J., et al. 2020, ApJ, 897, 93
Botteon, A., Shimwell, T. W., Cassano, R., et al. 2022, A&A, 660, A78
Botteon, A., Markevitch, M., van Weeren, R. J., Brunetti, G., & Shimwell, T. W. 2023, A&A, 674, A53
Boxelaar, J. M., van Weeren, R. J., & Botteon, A. 2021, Astron. Comput., 35, 100464
Briggs, D. S. 1995, PhD Thesis, New Mexico Institute of Mining and Technology, USA
Brunetti, G., & Jones, T. W. 2014, Int. J. Mod. Phys. D, 23, 1430007
Brunetti, G., Giacintucci, S., Cassano, R., et al. 2008, Nature, 455, 944
Brunetti, G., Zimmer, S., & Zandanel, F. 2017, MNRAS, 472, 1506
Bruno, L., Botteon, A., Shimwell, T., et al. 2023a, A&A, 678, A133
Bruno, L., Brunetti, G., Botteon, A., et al. 2023b, A&A, 672, A41
Campitiello, M. G., Ettori, S., Lovisari, L., et al. 2022, A&A, 665, A117
Cassano, R., Gitti, M., & Brunetti, G. 2008, A&A, 486, L31
Cassano, R., Ettori, S., Giacintucci, S., et al. 2010, ApJ, 721, L82
Cassano, R., Ettori, S., Brunetti, G., et al. 2013, ApJ, 777, 141
Cassano, R., Cuciti, V., Brunetti, G., et al. 2023, A&A, 672, A43
Castagné, D., Soucail, G., Pointecouteau, E., et al. 2012, A&A, 548, A18
Cavaliere, A., & Fusco-Femiano, R. 1976, A&A, 49, 137
CHEX-MATE Collaboration (Arnaud, M., et al.) 2021, A&A, 650, A104
Cuciti, V., Cassano, R., Brunetti, G., et al. 2015, A&A, 580, A97
Cuciti, V., Cassano, R., Brunetti, G., et al. 2021, A&A, 647, A51
Cuciti, V., de Gasperin, F., Brüggen, M., et al. 2022, Nature, 609, 911
De Luca, A., & Molendi, S. 2004, A&A, 419, 837
Duchesne, S. W., Johnston-Hollitt, M., & Bartalucci, I. 2021, PASA, 38, e053
Feretti, L., Fusco-Femiano, R., Giovannini, G., & Govoni, F. 2001, A&A, 373, 106
Forman, W., & Jones, C. 1982, ARA&A, 20, 547
Giacintucci, S., Venturi, T., Brunetti, G., et al. 2005, A&A, 440, 867
Giacintucci, S., Markevitch, M., Cassano, R., et al. 2017, ApJ, 841, 71
Gitti, M., Brunetti, G., Setti, G., & Feretti, L. 2004, in The Riddle of Cooling Flows in Galaxies and Clusters of Galaxies, eds. T. Reiprich, J. Kempner, & N. Soker, 35
Gitti, M., Brighenti, F., & McNamara, B. R. 2012, Adv. Astron., 2012, 950641P
Gitti, M., Brunetti, G., Cassano, R., & Ettori, S. 2018, A&A, 617, A11
Govoni, F., Enßlin, T. A., Feretti, L., & Giovannini, G. 2001, A&A, 369, 441
Govoni, F., Murgia, M., Markevitch, M., et al. 2009, A&A, 499, 371
Hudson, D. S., Mittal, R., Reiprich, T. H., et al. 2010, A&A, 513, A37
Ignesti, A., Brunetti, G., Gitti, M., & Giacintucci, S. 2020, A&A, 640, A37
Jacob, S., & Pfrommer, C. 2017, MNRAS, 467, 1478
Kelly, B. C. 2007, ApJ, 665, 1489
Kuntz, K. D., & Snowden, S. L. 2008, A&A, 478, 575
LaRoque, S. J., Bonamente, M., Carlstrom, J. E., et al. 2006, ApJ, 652, 917
Lovisari, L., & Reiprich, T. H. 2019, MNRAS, 483, 540
Lovisari, L., Schindler, S., & Kapferer, W. 2011, A&A, 528, A60
Lovisari, L., Forman, W. R., Jones, C., et al. 2017, ApJ, 846, 51
Madsen, K. K., Beardmore, A. P., Forster, K., et al. 2017, AJ, 153, 2
Mann, A. W., & Ebeling, H. 2012, MNRAS, 420, 2120
Mohr, J. J., Evrard, A. E., Fabricant, D. G., & Geller, M. J. 1995, ApJ, 447, 8
Mohr, J. J., Mathiesen, B., & Evrard, A. E. 1999, ApJ, 517, 627
Murgia, M., Govoni, F., Markevitch, M., et al. 2009, A&A, 499, 679
Nevalainen, J., Markevitch, M., & Lumb, D. 2005, ApJ, 629, 172
Offringa, A. R., McKinley, B., Hurley-Walker, N., et al. 2014, MNRAS, 444, 606
Pasini, T., Gitti, M., Brighenti, F., et al. 2019, ApJ, 885, 111
Pasini, T., Finoguenov, A., Brüggen, M., et al. 2021, MNRAS, 505, 2628
Paturel, G., Fouqué, P., Bottinelli, L., & Gouguenheim, L. 1989, Catalogue of Principal Galaxies. Vol. 1: Introduction and finding list. Vol. 2: Galaxies between 0h and 11h47m57s-5 in right ascension (2000). Vol. 3: Galaxies between 11h47m57s-7 and 24h in right ascension (2000)
Pfrommer, C., & Enßlin, T. A. 2004, A&A, 413, 17
Planck Collaboration XXIX. 2014, A&A, 571, A29
Planck Collaboration XXVII. 2016, A&A, 594, A27
Poole, G. B., Fardal, M. A., Babul, A., et al. 2006, MNRAS, 373, 881
Pratt, G. W., & Arnaud, M. 2002, A&A, 394, 375
Pratt, G. W., Böhringer, H., Croston, J. H., et al. 2007, A&A, 461, 71
Rajpurohit, K., Vazza, F., van Weeren, R. J., et al. 2021, A&A, 654, A41
Rawle, T. D., Edge, A. C., Egami, E., et al. 2012, ApJ, 747, 29
Riseley, C. J., Bonnassieux, E., Vernstrom, T., et al. 2022a, MNRAS, 515, 1871
Riseley, C. J., Rajpurohit, K., Loi, F., et al. 2022b, MNRAS, 512, 4210
Riseley, C. J., Biava, N., Lusetti, G., et al. 2023, MNRAS, 524, 6052
Robitaille, T., & Bressert, E. 2012, Astrophysics Source Code Library [record ascl:1208.017]
Rossetti, M., Gastaldello, F., Ferioli, G., et al. 2016, MNRAS, 457, 4515
Santos, J. S., Rosati, P., Tozzi, P., et al. 2008, A&A, 483, 35
Sarazin, C. L. 2009, X-Ray Emission from Clusters of Galaxies (Cambridge: Cambridge University Press)
Savini, F., Bonafede, A., Brüggen, M., et al. 2018, MNRAS, 478, 2234
Savini, F., Bonafede, A., Brüggen, M., et al. 2019, A&A, 622, A24
Shimwell, T. W., Röttgering, H. J. A., Best, P. N., et al. 2017, A&A, 598, A104
Shimwell, T. W., Tasse, C., Hardcastle, M. J., et al. 2019, A&A, 622, A1
Shimwell, T. W., Hardcastle, M. J., Tasse, C., et al. 2022, A&A, 659, A1
Smith, R. K., Brickhouse, N. S., Liedahl, D. A., & Raymond, J. C. 2001, ApJ, 556, L91
Snowden, S. L., Mushotzky, R. F., Kuntz, K. D., & Davis, D. S. 2008, A&A, 478, 615
Sommer, M. W., Basu, K., Intema, H., et al. 2017, MNRAS, 466, 996
Sutherland, R. S., & Dopita, M. A. 1993, ApJS, 88, 253
Tasse, C., Shimwell, T., Hardcastle, M. J., et al. 2021, A&A, 648, A1
van den Bosch, F. C., Weinmann, S. M., Yang, X., et al. 2005, MNRAS, 361, 1203
van der Walt, S., Colbert, S. C., & Varoquaux, G. 2011, Comput. Sci. Eng., 13, 22
van Haarlem, M. P., Wise, M. W., Gunst, A. W., et al. 2013, A&A, 556, A2
van Weeren, R. J., de Gasperin, F., Akamatsu, H., et al. 2019, Space Sci. Rev., 215, 16
van Weeren, R. J., Shimwell, T. W., Botteon, A., et al. 2021, A&A, 651, A115
Venturi, T., Rossetti, M., Brunetti, G., et al. 2017, A&A, 603, A125
Vikhlinin, A., Markevitch, M., Murray, S. S., et al. 2005, ApJ, 628, 655
Willingale, R., Starling, R. L. C., Beardmore, A. P., Tanvir, N. R., & O'Brien, P. T. 2013, MNRAS, 431, 394
Yuan, Z. S., Han, J. L., & Wen, Z. L. 2022, MNRAS, 513, 3013
Zhang, Y.-Y., Reiprich, T. H., Finoguenov, A., Hudson, D. S., & Sarazin, C. L. 2009, ApJ, 699, 1178

Appendix A: Flux Density CAlculator results

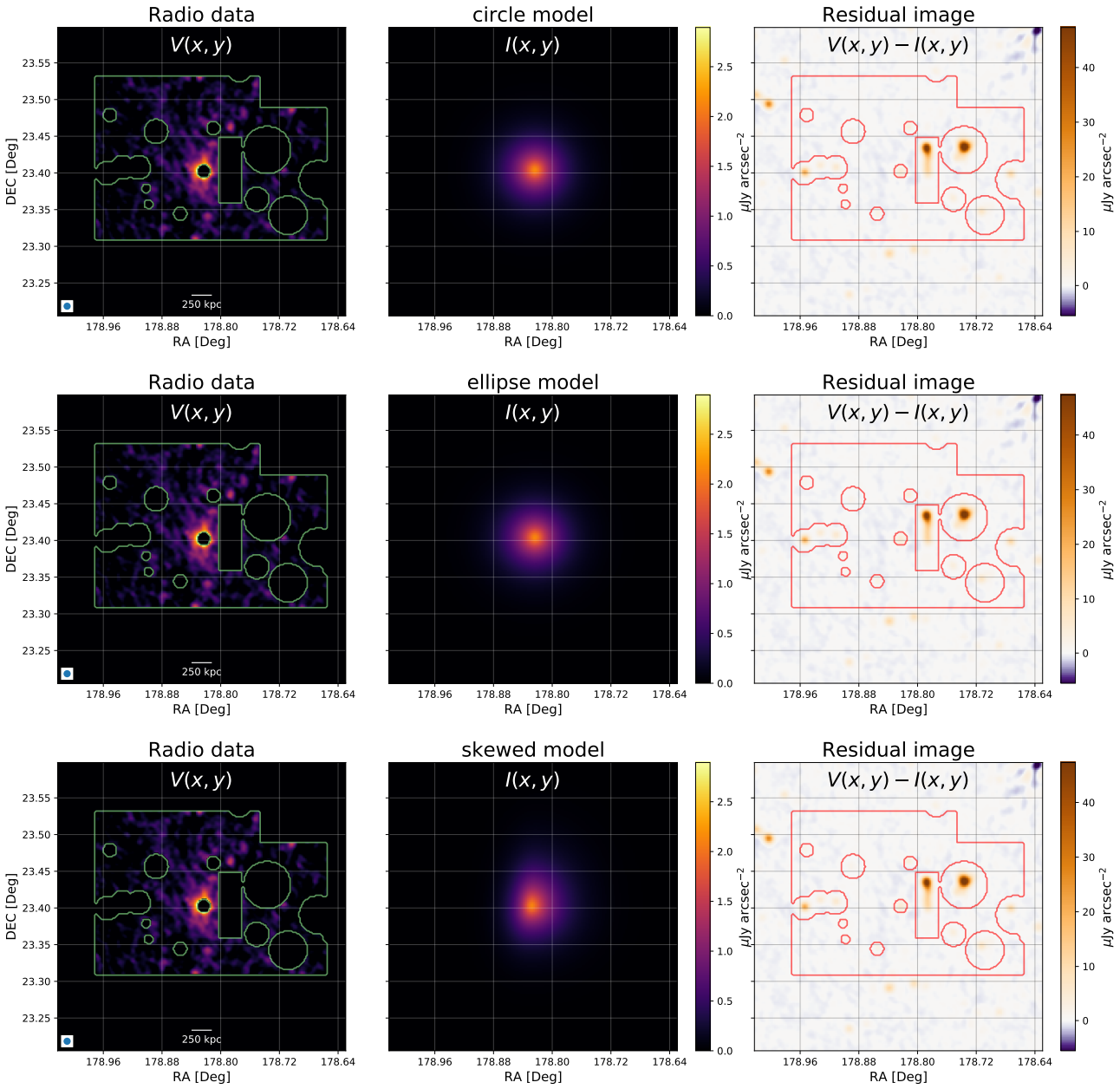

Fig. A.1. `FDCA-Halo` results for the radio halo in A1413 at 144 MHz frequency. Left panel: original image with the contaminating regions masked out. Middle panel: circular model map. Right panel: residual image. The red contours show the masked regions; the contamination sources are visible.